Inorganic Chemistry

pubs.acs.org/IC Article

Supramolecular Catalysis of Acyl Transfer within Zinc Porphyrin-Based Metal–Organic Cages

LiLi Li, Linlin Yang, Xuezhao Li, Jing Wang, Xin Liu,* and Cheng He*

Cite This: *Inorg. Chem.* 2021, 60, 8802–8810 Read Online

ACCESS | Metrics & More | Article Recommendations | Supporting Information

ABSTRACT: To illustrate the supramolecular catalysis process in molecular containers, two porphyrinatozinc(II)-faced cubic cages with different sizes were synthesized and used to catalyze acyl-transfer reactions between *N*-acetylimidazole (NAI) and various pyridylcarbinol (PC) regioisomers (2-PC, 3-PC, and 4-PC). A systemic investigation of the supramolecular catalysis occurring within these two hosts was performed, in combination with a host–guest binding study and density functional theory calculations. Compared to the reaction in a bulk solvent, the results that the reaction of 2-PC was found to be highly efficient with high rate enhancements (k_{cat}/k_{uncat} = 283 for **Zn-1** and 442 for **Zn-2**), as well as the different efficiencies of the reactions with various ortho-substituted 2-PC substrates and NAI derivates should be attributed to the cages having preconcentrated and preoriented substrates. The same cage displayed different catalytic activities toward different PC regioisomers, which should be mainly attributed to different binding affinities between the respective reactant and product with the cages. Furthermore, control experiments were carried out to learn the effect of varying reactant concentrations and product inhibition. The results all suggested that, besides the confinement effect caused by the inner microenvironment, substrate transfer, including the encapsulation of the reactant and the release of products, should be considered to be a quite important factor in supramolecular catalysis within a molecular container.

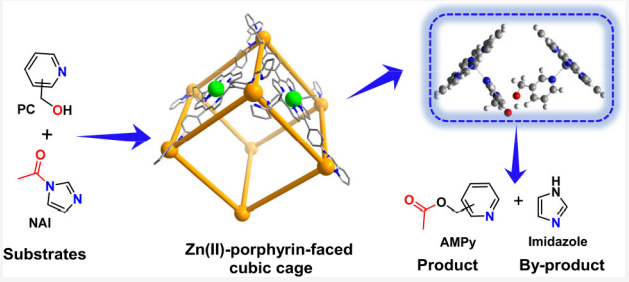

INTRODUCTION

Inspired by the excellent catalytic performance of enzyme in nature, "molecular containers" with defined cavities and active sites have been constructed and employed to catalyze unique chemical transformations. Of such artificial containers, coordination-driven assembled metal–organic cages (MOCs), in particular, have drawn considerable attention because of their ability to accommodate guest molecules and realize chemical transformations.[1−9] On the basis of their relatively rigid and hydrophobic central cavities, the hosts provide a biomimetic approach to emulating the environment of enzyme pockets and active sites.[10−13]

For the supramolecular catalytic reaction within a molecular container, binding of the guests in the cage cavity driven by the hydrophobic effect or other noncovalent interactions is the initial step.[14] Then the orientation and motion of the guest within the confined cavity are restricted by their complementary shapes as well as the steric hindrance and noncovalent interactions between the guest and host,[15−17] especially for multimolecular reactions or reactions catalyzed through direct interactions between the reactant and host, and the arrangement and orientation of the substrates within the confined cavity have a great influence on the formation of the transition state.[18−21] At last, to be an efficient enzyme-like catalyst, it needs to be able to catalyze reactions by binding transition states and intermediates more strongly than the products.[22]

Compared to the molecular catalysis taking place in a bulk solution, it has been demonstrated that the "confinement effects" induced by the special microenvironment within the host cavities could successfully enhance the reaction rate through the preconcentration and preorientation of the substrates, as well as the stabilization of the intermediates.[23−25] Thus, for the supramolecular catalysis within the molecular containers, the substrate transfer, including the ingress of the reactants and the egress of the products, might become a considerable rate-limiting step. As pointed out, the factors that lead to efficient recognition of the transition state were often linked to tight binding of the product, many artificial catalysts often fail to achieve the catalytic cycle due to product inhibition, and only stoichiometric reactions, rather than catalytic reactions, have been performed in some coordination cages.[26−29]

In the past decades, the host–guest interaction has been well studied to elucidate the confinement effects within the

Received: March 11, 2021
Published: June 4, 2021

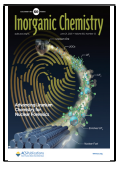

https://doi.org/10.1021/acs.inorgchem.1c00745
Inorg. Chem. 2021, 60, 8802–8810

Scheme 1. Illustration of the Self-Assembly of Cubic Cages (a) Zn-1 and (b) Zn-2

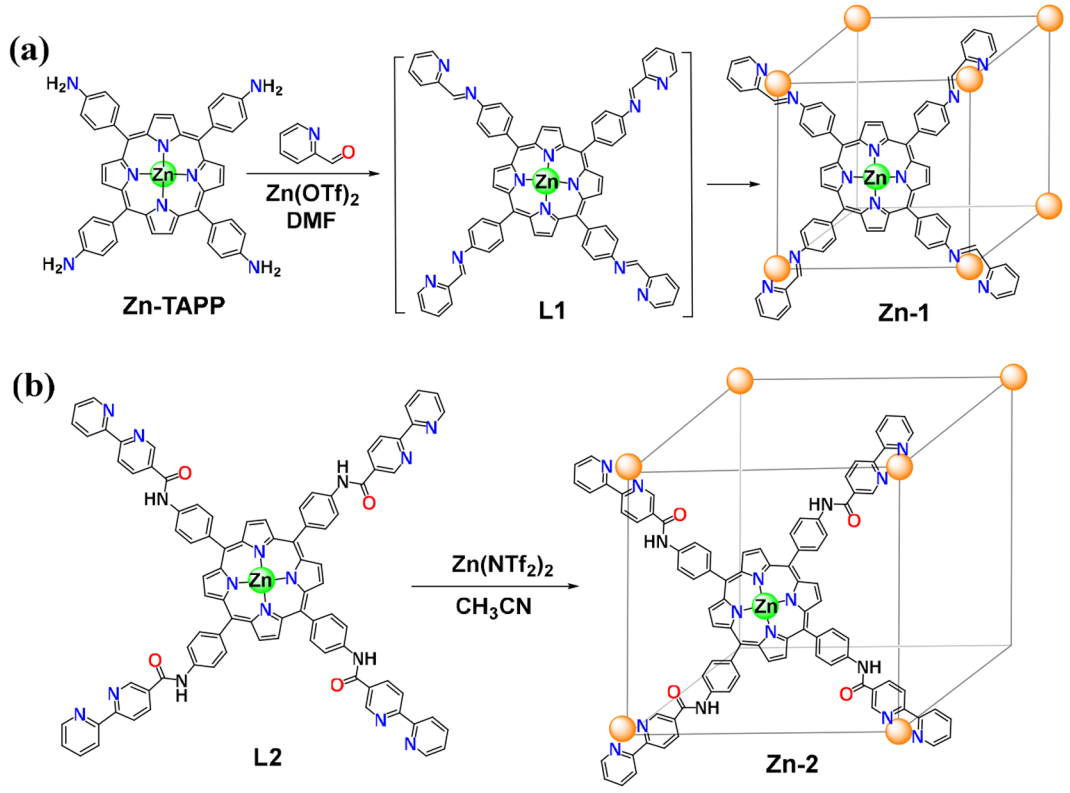

cages.[1−5,25] In order to allow for the design of an efficient supramolecular catalyst with an inner microenvironment isolated from the bulk solution, the substrate transfer needs to be carefully studied. Multimetalloporphyrin compounds have been shown to exhibit unique properties because of their spatial arrangement with respect to each other, and supramolecular MOCs containing multiple metalated porphyrin units offer a potentially facile route to biomimetic structures for supramolecular catalysis research.[30−36] We envisaged that the catalytic activity occurring within the host cavities could be influenced by the distance of the porphyrins if the reaction requires orientation-specific, concerted binding of the reactants by the metalated porphyrin centers. Herein, through regulation of the cavity size of two porphyrinatozinc(II)-faced cubic cages, a systemic investigation of the supramolecular catalysis based on the two host cages was performed. The homogeneous nature of coordination cages allows investigation of the catalytic properties and host−guest interaction in solvated media.

RESULTS AND DISCUSSION

Synthesis and Characterization of Cages. The ligand zinc(II) tetrakis(*p*-aminophenyl)porphyrin (Zn-TAPP) was synthesized according to the reported procedure,[37] and zinc(II) 5,10,15,20-tetraryltetrakis(benzene-4,1-diyl)tetrakis-(2,2′-bipyridine-5-carboxamide)porphine (**L2**) was synthesized by reacting Zn-TAPP with 2,2′-bipyridine-5-carboxyl chloride. As shown in Scheme 1, the cage **Zn-1** was prepared by a subcomponent self-assembly from Zn-TAPP (6 equiv), 2-formylpyridine (24 equiv), and $Zn(OTf)_2$ (8 equiv) in *N*,*N*-dimethylformamide (DMF) at 70 °C, according to the procedure reported by Nitschke and co-workers.[37−39] Different from **Zn-1**, the cage **Zn-2** was directly obtained by heating **L2** (6 equiv) and $Zn(NTf_2)_2$ (8 equiv) in CH_3CN at 70 °C in a sealed vessel. Single crystals of **Zn-1** were obtained by diffusion of diethyl ether into a mixture DMF solution.

Electrospray ionization mass spectrometry (ESI-MS) analysis suggested the formations and stability of **Zn-1** and **Zn-2** in solution. The spectrum of **Zn-1** showed peaks clearly displaying the expected isotopic patterns at *m*/*z* 712.30, 798.53, 903.91, 1035.40, 1204.60, and 1430.02 belonging to $[Zn_8(\mathbf{L1})_6{\cdot}n\mathrm{OTf}]^{(16-n)+}$ [*n* = 5−10; **L1** = zinc(II) 5,10,15,20-tetraryltetrakis(benzene-4,1-diyl)tetrakis(1-(pyridin-2-yl)-methanimine)porphine], respectively. Also peaks at *m*/*z* 781.96, 870.45, 975.12, 1100.33, 1253.91, 1445.63, and 1692.28 for **Zn-2** were observed and assigned to $[Zn_8(\mathbf{L2})_6{\cdot}n\mathrm{NTf_2}]^{(16-n)+}$ (*n* = 3−9) (Figure 1), respectively.

The formations of the two cages were further characterized by carrying out ^{1}H, ^{13}C, ^{19}F, ^{1}H COSY, and ^{1}H DOSY NMR analyses (Figures S1−S14). The ^{1}H and ^{13}C NMR spectra of each cage displayed only one set of ligand resonance signals in solution, which also confirmed the formation of a discrete and highly symmetric assembly. Most of these signals each showed a slight downfield shift with respect to the free ligand. A single peak was observed for each proton of the ligand, with ^{1}H−^{1}H COSY NMR data allowing the assignment of each signal. Additionally, a two-dimensional (2D) ^{1}H DOSY NMR technique was used, and from these experiments, the diffusion coefficient (*D*) values of **Zn-1** and **Zn-2** were determined to be 2.18×10^{-10} and 2.63×10^{-10} m^2 s^{-1}, respectively. ^{19}F NMR spectroscopy data showed no indication of encapsulation of the counterions by **Zn-1** or **Zn-2**.

A single-crystal X-ray diffraction study of **Zn-1** revealed the formation of a highly symmetric face-capped cubic cage (Figure 2a,b). **Zn-1** crystallized in the tetragonal space group *P*4/*n*, with one-fourth of the formula unit in the asymmetric

https://doi.org/10.1021/acs.inorgchem.1c00745
Inorg. Chem. 2021, 60, 8802−8810

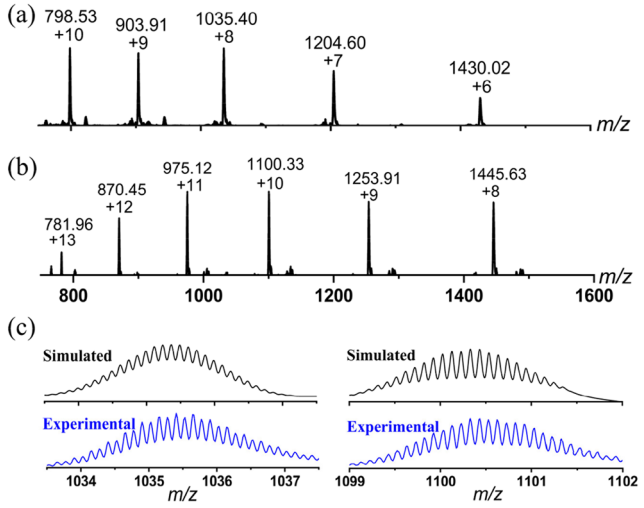

Figure 1. ESI-MS spectra of the synthesized cubic cages (a) **Zn-1** and (b) **Zn-2**. (c) Experimental and calculated peaks for $[\mathbf{Zn\text{-}1}\ (OTf)_8]^{8+}$ (left) and $[\mathbf{Zn\text{-}2}\ (NTf_2)_6]^{10+}$ (right).

unit. Each face of **Zn-1** was observed to be covered by one zinc porphyrin-based ligand, and each corner was observed to be occupied by a six-coordinate Zn(II) ion, with each corner Zn atom chelated by three ligands. The corner Zn atoms along the cage edges were measured to be separated by 14.90−15.17 Å. The cavity of the cage showed inner voids with volumes of about 1436 Å^3, large enough to encapsulate both of the *N*-acetylimidazole (NAI) and X-pyridylcarbinol (X-PC, where X = 2, 3, or 4) guests and allow the ingress and egress of the corresponding reactants and products. Zn−Zn distances of 14.48−15.74 Å were measured between the porphyrin centers of the opposite faces. Also Zn atoms on the adjacent faces were measured to be separated by 10.6 Å. The faces of the cubic cage did not form regular planes: of the three groups of the opposite faces, the faces of two of them were observed to display inward concave shapes and the faces of the third group formed outward protrusions. Unfortunately, weak X-ray diffraction limited the crystal structure determination of the **Zn-2** cage. Because ligand **L2** was prepared as a tetradentate ligand similar to ligand **L1** in **Zn-1**, **Zn-2** should also have cubic topology. A molecular mechanical (MM)-minimized model of **Zn-2** is shown in Figure 2c,d. This model shows porphyrin Zn−Zn distances of about 17.01 Å between the two opposite planes and of about 12.03 Å between the adjacent faces, larger than the corresponding distances in **Zn-1**. The adjacent porphyrin Zn−Zn distances in the two cages were comparable with those of the previously reported multi-metalloporphyrin compounds, which could efficiently catalyze the acyl-transfer reactions.[40−43]

Supramolecular Catalysis Study. The supramolecular catalysis behaviors of the cages were first evaluated by examining their catalysis of the acyl transfer reaction between NAI and 2-PC. As shown in Figure 3, both **Zn-1** and **Zn-2** significantly accelerated the reaction rate, with their initial reaction rates measured to be 3.5 and 4.6 mM h^{-1}, respectively. Control experiments showed that, in the absence of the cages, the reaction of 2-PC with NAI only gave an approximately 12.5% yield at 50 °C after 96 h (Table S4), and the apparent second-order rate constant for the uncatalyzed reaction was determined to be 2.26×10^{-5} M^{-1} s^{-1}. The k_{cat} (Michaelis−Menten enzymatic rate constant) values for **Zn-1** and **Zn-2** were found to be 6.4×10^{-3} and 1×10^{-2} M^{-1} s^{-1}, corresponding to an overall acceleration (k_{cat}/k_{uncat}) of 283 and 442, respectively (Figures S52 and S53). The efficiency of both the supramolecular catalysts (**Zn-1** and **Zn-2**) in the acyl-transfer reaction was also evaluated against the control reactions in which the cages were displaced by the monomers

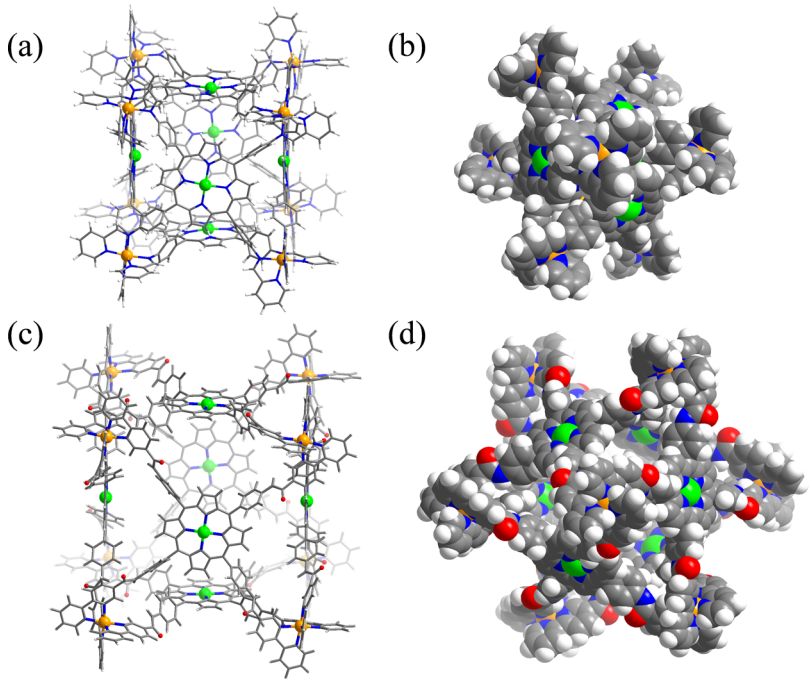

Figure 2. Perspective views of (a) the single-crystal X-ray structure of **Zn-1** and (c) the MM-minimized model of **Zn-2** and (b and d) their space-filling models. Color code: orange (corners) and green (face-centers), Zn; blue, N; gray, C; red, O; white, H. Disorder, anions, and solvent molecules are omitted for clarity.

https://doi.org/10.1021/acs.inorgchem.1c00745
Inorg. Chem. 2021, 60, 8802−8810

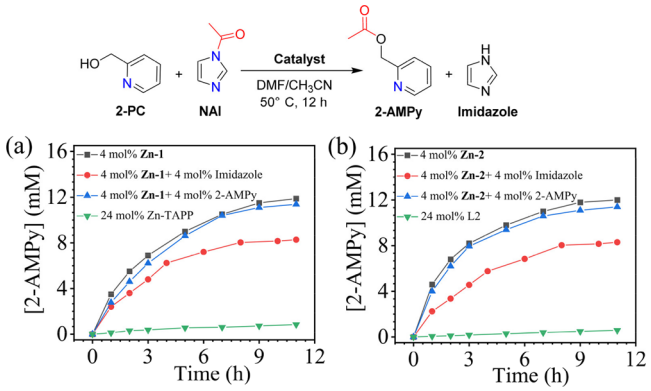

Figure 3. Kinetic data for the acyl-transfer reaction of 2-PC (18 mM) and NAI (12 mM) performed in the presence of (a) **Zn-1** (black squares), **Zn-1** together with 0.5 mM imidazole (red circles), **Zn-1** together with 0.5 mM 2-(acetoxymethyl)pyridine (2-AMPy) (blue triangles) and Zn-TAPP (green triangles) and (b) **Zn-2** (black squares), **Zn-2** together with 0.5 mM imidazole (red circles), **Zn-2** together with 0.5 mM 2-AMPy (blue triangles) and **L2** (green triangles).

Zn-TAPP and **L2**. In the presence of the monomer Zn-TAPP and **L2** (24 mol %), the initial rates of the transacylation only increased 4-fold and 2.5-fold, respectively. The reactions with varying concentrations of 2-PC and NAI are shown in Figure 4,

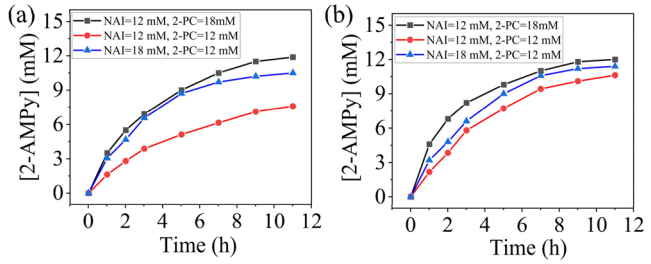

Figure 4. Kinetic data for the acyl-transfer reaction performed in various concentrations of substrates in the presence of (a) **Zn-1** and (b) **Zn-2**, respectively: [NAI] = 12 mM, [2-PC] = 18 mM (black squares); [NAI] = 12 mM, [2-PC] = 12 mM (red circles); [NAI] = 18 mM, [2-PC] = 12 mM (blue triangles).

and when 2-PC and NAI were both 12 mM, the reaction rates were 1.6 and 2.2 mM h^{-1} in **Zn-1** and **Zn-2**, respectively; at concentrations of 12 mM 2-PC and 18 mM NAI, the reaction rates were 3.0 and 3.2 mM h^{-1} in **Zn-1** and **Zn-2**, respectively.

To investigate the preconcentration effect of the cages, acyl-transfer reactions were carried out with other derivatives of 2-PC and NAI (Table 1). When the *m*-R^1 group in 2-PC was replaced with a large aromatic group (phenyl, biphenyl, anthryl, and so on), the **Zn-1** and **Zn-2** cages showed well activity toward the reaction, with good yields (over 90%, Table 1). When the substrate scope was further expanded to modifying R^3 (methyl or phenyl), i.e., that positioned ortho to the N atom of 2-PC, the yields of the reaction dramatically decreased (11−17% for **Zn-1** and 13−20% for **Zn-2**). In the case of NAI with an isopentyl R^2 group (**2e**), the substrate **2e** exhibited a small reduction of the yield.

The reaction rates of 3-PC and 4-PC in the given cage were significantly lower than those of 2-PC (Figure 5). For **Zn-1**, when using 3-PC, the acyl-transfer reaction proceeded at a medium rate (2.2 mM h^{-1}) and the rates for 4-PC was quite

Table 1. Acyl-Transfer Reactions of a Series of Substrates Catalyzed by the Cubic Cages[a]

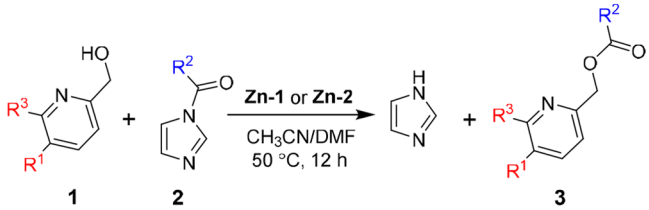

entry	catalyst	R^1	R^2	R^3	yield (%)
1	**Zn-1**	Ph	H	H	**3a**/96
2	**Zn-2**	Ph	H	H	**3a**/95
3	**Zn-1**	PhOMe	H	H	**3b**/93
4	**Zn-2**	PhOMe	H	H	**3b**/95
5	**Zn-1**	biphenyl	H	H	**3c**/90
6	**Zn-2**	biphenyl	H	H	**3c**/95
7	**Zn-1**	anthryl	H	H	**3d**/91
8	**Zn-2**	anthryl	H	H	**3d**/94
9	**Zn-1**	H	isopentyl	H	**3e**/80
10	**Zn-2**	H	isopentyl	H	**3e**/84
11	**Zn-1**	H	H	Me	**3f**/17
12	**Zn-2**	H	H	Me	**3f**/20
13	**Zn-1**	H	H	Ph	**3g**/11
14	**Zn-2**	H	H	Ph	**3g**/13

[a]Reation conditions: catalyst (0.5 mM, 4 mol %), **1** (18 mM), **2** (12 mM), CH_3CN/DMF [3:1 (v/v), 4 mL], 50 °C. All yields were determined by GC analysis.

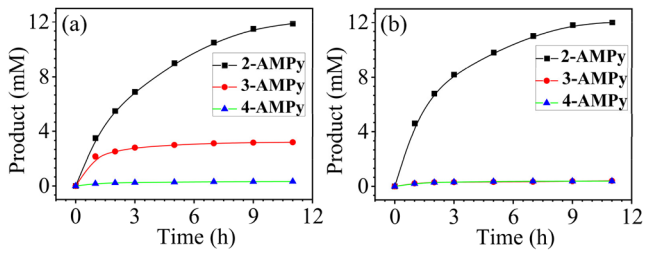

Figure 5. Formation of the three X-(acetoxymethyl)pyridine (AMPy, where X = 2, 3, or 4) isomers from acyl-transfer reactions between 1-acetylimidazole and X-PC, as catalyzed by (a) **Zn-1** and (b) **Zn-2**. Concentration versus time plots are shown for the formation of 2-AMPy (black squares), 3-AMPy (red circles), and 4-AMPy (blue triangles).

lower (0.17 mM h^{-1}). Interestingly, although the reaction of 2-PC catalyzed by **Zn-2** had a higher rate than that by **Zn-1**, **Zn-2** just showed fairly low catalytic activity toward both 3-PC and 4-PC, with the reaction rates being only 0.22 and 0.20 mM h^{-1}, respectively.

Finally, to a solution of **Zn-1** or **Zn-2** (0.5 mM) in CH_3CN/DMF (3:1 in volume), we added several successive portions of NAI and 2-PC, waiting until each aliquot had completely reacted before adding the next. The total turnover numbers for **Zn-1** and **Zn-2** could reach 158 and 162, respectively. Also, with the product increased, the yields decreased from 91.5% to 55.0% for **Zn-1** and from 98.8% to 60.0% for **Zn-2** during the course of five times (Figure 6).

Host−Guest Binding Study. The binding constants of each substrate with **Zn-1** or **Zn-2** were then determined by performing UV−vis titration, using a noncooperative 1:1 host−guest binding model. As shown in Table 2, the substrate NAI binds well to **Zn-1** (K_a = 1224 M^{-1}) and **Zn-2** (K_a = 4000

https://doi.org/10.1021/acs.inorgchem.1c00745
Inorg. Chem. 2021, 60, 8802−8810

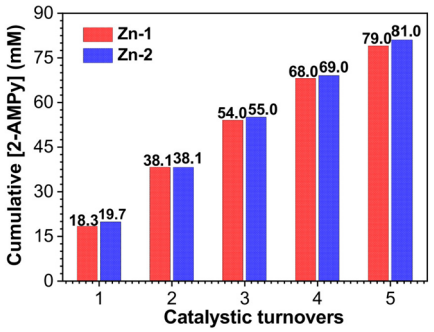

Figure 6. Demonstration of catalytic turnover with **Zn-1** (red bar) and **Zn-2** (blue bar). The graph shows the accumulation of 2-AMPy following the addition of a series of aliquots of substrates (NAI, 20 mM; 2-PC, 30 mM) to a solution of **Zn-1** (0.5 mM) and **Zn-2** (0.5 mM) in 3:1 CH_3CN/DMF. Aliquots of the substrate were added at 12 h intervals.

M^{-1}), and the substrate 2-PC exhibits weak binding for **Zn-1** (K_a = 262 M^{-1}) and **Zn-2** (K_a = 200 M^{-1}). For the meta-position-substituted 2-PCs, the affinity changed little or became stronger, possibly due to the $\pi\cdots\pi$ interactions (Figures S41 and S42). The ortho-position-substituted 2-PC showed negligible binding toward the two cages (Figures S33–S36). Also the NAI derivate **2e** bound less well to the cages, with K_a values of 213 and 333 M^{-1} for **Zn-1** and **Zn-2**, respectively (Figures S43 and S44).

For the relative products, the UV–vis absorption spectrum of **Zn-1** changed very little upon the addition of 2-AMPy to **Zn-1**, indicating the weak interaction between them. The corresponding product **3e** also showed very weak interaction with the two cages (Figures S45 and S46). **Zn-1** also appeared to show a weak affinity for 3-AMPy (K_a = 256 M^{-1}) but a high affinity for 4-AMPy (K_a = 1607 M^{-1}). **Zn-2** tightly bound 3-AMPy (K_a = 1100 M^{-1}) and 4-AMPy (K_a = 1000 M^{-1}) but showed poorer binding of 2-AMPy. The binding affinities of the byproduct imidazole in **Zn-1** or **Zn-2** were similar.

Computational Modeling. The orientation effect for the formation of the respective transition state of each regioisomer was then investigated by density functional theory (DFT)-based calculations (Figure 7). Because only Zn(II) on the faces of cationic cages can bind the organic substrates and products, the cages were then simplified as two zinc(II) porphyrins nearly vertical to each other to make the calculations efficient. The reaction mechanisms of formation of the transition state between each organic substrate were then investigated with specific D_{Zn-Zn} values at 10.06 and 12.03 Å of **Zn-1** and **Zn-2**, respectively. For **Zn-1**, the barriers to formation and dissociation of the proton-transfer intermediates were 35.45 and 32.15 kcal mol^{-1}, respectively, on the reaction path to 2-AMPy, 43.46 and 43.65 kcal mol^{-1}, respectively, on the path to 3-AMPy, and 44.85 and 37.10 kcal mol^{-1}, respectively, on the path to 4-AMPy. For **Zn-2**, the barriers to formation and dissociation of the proton-transfer intermediates were 47.25 and 41.01 kcal mol^{-1}, respectively, on the reaction path to 2-AMPy, 41.41 and 39.87 kcal mol^{-1}, respectively, on the path to 3-AMPy, and 46.51 and 38.76 kcal mol^{-1}, respectively, on the path to 4-AMPy.

DISCUSSION

Two zinc porphyrin-based MOCs (**Zn-1** and **Zn-2**) having the same cubic topology but different sizes were constructed by adjusting the length of their ligands, and their rate accelerations were quite comparable to those reported for supramolecular catalysis in metal–organic hosts.[40−46] As was well studied in previous works,[40−42,46,47] the supramolecular catalytic process including preorganization of the two substrates via their simultaneous encapsulation within a single cavity led to the formation of a suitable transition state by fixing the positions and orientations of the hydroxyl and carbonyl moieties of the respective substrates, resulting in a significant rate acceleration.

Increasing the size of R^3 did increase the steric hindrance of the N atom of 2-PC and was hence not beneficial for encapsulation of the substrates within the cages (**1f** and **1g** negligible binding toward the two cages). The NAI derivate **2e**, which show a lower affinity to the cage, also resulted in lower yield (the steric hindrance of the carbonyl sites also affects formation of the transition state). In these cases, the predominant factor affecting the reaction efficiency for the corresponding reaction would be expected to be the preconcentration effect.

The reaction rate was found to be quite sensitive to the different regioisomers (Figure 5). For both **Zn-1** and **Zn-2**, 2-PC showed the highest reaction efficiency, while 2-PC showed lower affinities toward the two cages than did 3-PC and 4-PC, suggesting that the lower reaction rates observed for 3-PC and 4-PC could not be attributed to the preconcentration effects. Then DFT-based calculations were undertaken to elucidate the orientation effect of the cages. Compared to the previous work reported by Deria and co-workers,[40] the distance between the opposite plane seems too far to contribute to the orientation effect, while the adjacent Zn centers (10.06 Å in **Zn-1** and 12.03 Å in **Zn-2**) should be the main active pairs. According to the DFT-calculated results, the faster reaction rate of 2-PC in **Zn-1** refers to the fact that those of 3-PC and 4-PC might be partly due to the orientation effect. However, it is hard to attribute the difference in the reaction rate to the orientation effect because of the limited difference in the reaction barriers for the transition state formation of the 3-PC and 4-PC regioisomers in the given cage. Also for catalysis to occur in **Zn-2**, the orientation effect could not be responsible for the high reaction rate of 2-PC.

Obviously, in addition to substrate binding and intermediate formation, product release should be considered as a key factor in these catalytic processes. It could be found that, in the case

Table 2. Association Constants Determined by Means of UV–Vis Spectroscopy

K_a (M^{-1})[a]	2-PC	3-PC	4-PC	NAI	2-AMPy[b]	3-AMPy	4-AMPy	imidazole
Zn-1	262	467	470	1224		256	1607	1160
Zn-2	200	333	438	4000		1100	1000	1000

[a]The interaction of these guests with hosts was studied in a 3:1 mixture of CH_3CN/DMF. The values of K_a were calculated using a noncooperative 1:1 binding model. [b]Because of the weak interaction between 2-AMPy and **Zn-1** or **Zn-2** and the negligible change of the UV–vis spectra, the value of K_a cannot be determined.

https://doi.org/10.1021/acs.inorgchem.1c00745
Inorg. Chem. 2021, 60, 8802−8810

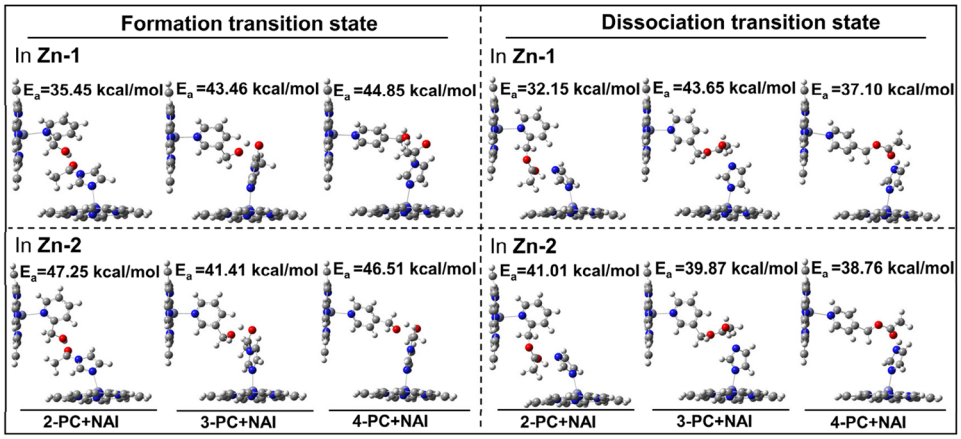

Figure 7. DFT calculation of the formation (left) and dissociation (right) transition states of the acyl-transfer reaction between PC (2-PC, 3-PC, and 4-PC, from left to right) and NAI in the cubic cages **Zn-1** and **Zn-2**, respectively.

in which the binding affinity of the respective reactant in the cages was weaker than that of the product X-AMPy, the related catalytic reaction just showed quite slow rates. The high catalytic efficiency of 2-PC might be greatly attributed to the fact that the product 2-AMPy was easily expelled from the cages, while that of the reaction of 3-PC in cage **Zn-1** gave a moderate rate that was also consistent with the fact that the binding affinity of 3-PC was larger than that of 3-AMPy with the cage.

To further confirm the impact of the release of products on the catalytic reaction, we conducted a control experiment in which 2-AMPy (0.5 mM) or imidazole (0.5 mM) was added to the reaction mixture, respectively. As shown in Figure 3, the addition of 2-AMPy, which binds very weakly to the cages, hardly influences the rate of the reaction in **Zn-1** and **Zn-2**, respectively, while upon inclusion of the imidazole, which binds tightly to these cages, the initial reaction rate decreased from 3.5 to 2.4 mM h^{-1} for **Zn-1** and from 4.6 to 2.2 mM h^{-1} for **Zn-2**. Notably, the larger affinity of the imidazole toward **Zn-2** resulted in the fact that the addition of the product reduced the initial rate of the reaction in **Zn-2** to a larger degree (52%) compared to that in **Zn-1** (31%).

The ingress of the reactants would also affect the reaction rates. The higher initial rate of the reaction for 2-PC in **Zn-2** than that in **Zn-1** seems better to be attributed to the affinity of NAI in **Zn-2** being stronger than that in **Zn-1**. Also, it could be found in Figure 4, in both **Zn-1** and **Zn-2**, that increasing the concentration of 2-PC from 12 to 18 mM could enhance the initial rates of the reactions to a larger degree than increasing the concentration of NAI on the same scale, and this could be explained as the encapsulation of the more weakly bound substrate 2-PC was the slower step of the reactions.

CONCLUSIONS

In summary, two self-assembled zinc porphyrin-faced cubic cages, **Zn-1** and **Zn-2**, with different cavity sizes were designed to catalyze transfer of the acyl group between NAI and PC for each of the three PC regioisomers (2-PC, 3-PC, and 4-PC). The supramolecular catalysis based on the cages was carefully studied through a series of control experiments, a host−guest binding study, and DFT-based calculations. **Zn-1** and **Zn-2** exhibited excellent activity (with k_{cat}/k_{uncat} = 283 for **Zn-1** and 442 for **Zn-2**) for 2-PC and NAI as reactants, with these activity levels attributable to the orientation effect for formation of the transition state based on the adjacent porphyrin Zn centers. Also the ortho-substituted 2-PC substrate with its sterically hindering group, one impending coordination of the substrate to the porphyrin Zn centers, led to dramatically decreased yields of the reaction, indicating that the preconcentration effect is based on the binding affinity of reactants and hosts. The catalytic activity was shown to vary for different PC regioisomers, an observation attributed to the X-AMPy products inhibiting the host as a result of the binding between these products and the hosts. The host−guest interaction study showed that the product 2-AMPy can be fairly easily expelled from the cage cavities to allow multiple catalytic turnovers but that 3-AMPy and 4-AMPy bind with the zinc porphyrin cubic capsule systems more tightly. The results illustrated that, in the case of supramolecular catalysis performed in a molecular container, when the reaction was efficiently accelerated through enhancement of the local concentration and stabilization of the transition state, which take advantage of the confinement effect, the substrate transfer between the inner and outer spaces of the container might become a considerable rate-limiting step of the reaction process. Our research shed light on the possible impact factors involved in each step of the supramolecular catalysis, which would be helpful for the development of artificial enzyme-like catalysts.

EXPERIMENTAL SECTION

Preparation of Zn-1. A mixture of Zn-TAPP (73.6 mg, 0.1 mmol), 2-formylpyridine (37 μL, 0.4 mmol), and $Zn(OTf)_2$ (48.3 mg, 0.133 mmol) was dissolved in 30 mL of DMF and then heated at 70 °C for 12 h to give a clear solution. The vapor of diethyl ether was allowed to diffuse slowly into a DMF solution of the reaction mixture. Block-shaped dark-purple crystals formed after 1 week in 76.0% yield (120.0 mg). Anal. Calcd for $C_{420}H_{264}N_{72}O_{48}F_{48}Zn_{14}S_{16}\cdot 8C_4H_{10}O\cdot 6C_3H_7NO\cdot 4H_2O$: C, 53.81; H, 3.75; N, 10.32. Found: C, 53.72; H, 3.86; N, 10.28. ^{1}H NMR (3:2 CD_3CN/DMF, 500 MHz): δ 9.50 (24H, s), 9.29 (24H, s), 8.86 (24H, d, J = 5.0 Hz), 8.67−8.63 (48H, m), 8.57(24H, d, J = 5.0 Hz), 8.15 (48H, s), 7.79 (24H, d, J = 5.0 Hz), 6.85 (24H, s), 6.38 (24H, s). ^{13}C NMR (3:2 CD_3CN/DMF, 500 MHz): δ 166.71, 162.85, 150.76, 150.11, 149.87, 147.64, 143.49, 142.73, 136.59, 135.79, 132.27, 132.07, 131.77, 131.65, 123.38, 120.47, 120.18, 119.88. ^{19}F NMR (3:2 CD_3CN/DMF, 500 MHz): δ 79.00. IR (KBr pellet, ν/cm^{-1}): 1631 (s), 1595 (s), 1523 (w), 1489 (m), 1443 (w), 1337 (w), 1263 (vs), 1169 (m), 1031 (s), 995 (m), 914 (w), 856 (w), 812 (w), 794 (w), 777 (w), 748 (w), 719 (w), 682 (w), 640 (m), 574 (w), 516 (w), 474 (w), 428 (w). ESI-MS: m/z

https://doi.org/10.1021/acs.inorgchem.1c00745
Inorg. Chem. 2021, 60, 8802−8810

712.30 ($[Zn_8(\mathbf{L1})_6(OTf)_5]^{11+}$), 798.53 ($[Zn_8(\mathbf{L1})_6(OTf)_6]^{10+}$), 903.91 ($[Zn_8(\mathbf{L1})_6(OTf)_7]^{9+}$), 1035.40 ($[Zn_8(\mathbf{L1})_6(OTf)_8]^{8+}$), 1204.60 ($[Zn_8(\mathbf{L1})_6(OTf)_9]^{7+}$), 1430.02 ($[Zn_8(\mathbf{L1})_6(OTf)_{10}]^{6+}$).

Preparation of Zn-2. A mixture of **L2** (87.8 mg, 0.06 mmol) and zinc bis(trifluoromethane sulfonimide) (50.0 mg, 0.08 mmol) was suspended in 20 mL of CH_3CN in a sealed vessel. The reaction mixture was heated at 70 °C for 16 h. This solution was added to diethyl ether, and the product was obtained after centrifugation and then dried. The desired product was obtained as a purple solid in 85.0% yield (117.1 mg). Anal. Calcd for $C_{560}H_{336}N_{112}O_{88}F_{96}S_{32}Zn_{14}\cdot 4H_2O$: C, 48.46; H, 2.50; N, 11.30. Found: C, 48.42; H, 2.56; N, 11.24. ^{1}H NMR (CD_3CN, 500 MHz): δ 9.59 (24H, s), 9.39 (24H, s), 8.99 (48H, s), 8.96 (24H, d, J = 10.0 Hz), 8.92 (24H, d, J = 5.0 Hz), 8.76 (24H, d, J = 5 Hz), 8.68 (24H, d, J = 5 Hz), 8.45 (24H, t, J = 5 Hz), 8.33 (48H, d, J = 5 Hz), 8.26 (48H, d, J = 5 Hz), 7.97 (24H, t, J = 5 Hz). ^{13}C NMR (CD_3CN, 500 MHz): δ 163.24, 150.84, 148.80, 148.15, 142.82, 140.31, 140.31, 138.47, 135.56, 134.47, 132.38, 128.55, 124.40, 124.21, 123.15, 119.38, 116.75. ^{19}F NMR (CD_3CN, 500 MHz): δ 80.15. IR (KBr pellet, ν/cm^{-1}): 1658 (s), 1602 (m), 1527 (s), 1475 (w), 1440 (w), 1402 (w), 1348 (s), 1197 (vs), 1135 (s), 1054 (s), 997 (m), 904 (w), 856 (w), 798 (w), 758 (w), 738 (w), 655 (w), 613 (w), 570 (w), 509 (w). ESI-MS: m/z 781.96 ($[Zn_8(\mathbf{L2})_6(NTf_2)_3]^{13+}$), 870.45 ($[Zn_8(\mathbf{L2})_6(NTf_2)_4]^{12+}$), 975.12 ($[Zn_8(\mathbf{L2})_6(NTf_2)_5]^{11+}$), 1100.33 ($[Zn_8(\mathbf{L2})_6(NTf_2)_6]^{10+}$), 1253.91 ($[Zn_8(\mathbf{L2})_6(NTf_2)_7]^{9+}$), 1445.63 ($[Zn_8(\mathbf{L2})_6(NTf_2)_8]^{8+}$), 1692.28 ($[Zn_8(\mathbf{L2})_6(NTf_2)_9]^{7+}$).

General Procedure for the Cage-Based Catalysis. To a solvent mixture of CH_3CN and DMF [3:1 (v/v), 4 mL] were added CH_3CN stock solutions of NAI (12 mM), PC (18 mM), and biphenyl (5 mM solution) and **Zn-1** (21.1 mg, 0.5 mM) or **Zn-2** (27.7 mg, 0.5 mM). The mixture solution was stirred at 50 °C for 12 h. At various times, an aliquot (50 μL) was taken from the solution and added to diethyl ether (1 mL), which was then passed through a filter membrane (0.22 mm) to remove the catalyst. The formation of products was monitored by gas chromatography (GC) relative to an internal standard (biphenyl). The pure products were obtained using column chromatography and characterized using ^{1}H and ^{13}C NMR.

General Procedure for Examination of the Multiple Turnover Catalysis. To a solution of 0.5 mM of each cage in CH_3CN/DMF (3:1 in volume), we added several successive portions of NAI (20 mM) and 2-PC (30 mM), stirring each one for 12 h at 50 °C before adding the next portion.

Molecular Simulations. DFT-based calculations, with the full-electron Gaussian-type basis sets developed by Collins and Hehre for C, N, and H atoms[48,49] together with Los Alamos effective core potentials developed by Hay, Wadt, and co-workers,[50−52] in conjunction with the B3LYP functional,[53,54] as implemented in *Gaussian 16*, revision A03,[55] were performed to understand the mechanisms for the acyl-transfer reactions.

Host−Guest Chemistry Studied Using UV−Vis Spectroscopy. A solution of **Zn-1** or **Zn-2** in CH_3CN/DMF (3:1 in volume; 3 mL, 0.5 or 0.25 μM) was transferred to a cuvette. Small aliquots of the guest solution were titrated into the cuvette. The experiment was performed at room temperature. Using nonlinear analysis with the *DynaFit* program (Biokin Software),[56] the binding equation derived for a 1:1 model (noncooperative model) was then fitted to the data obtained from the UV−vis titration.

Crystallography. The X-ray intensities of the complexes were collected on a Bruker SMART APEX CCD diffractometer with graphite-monochromated Mo Kα (λ = 0.71073 Å) using the *SMART* and *SAINT* programs.[57,58] The structures were solved by direct methods and refined on F^2 by full-matrix least-squares methods with *SHELXTL-2018*.[59]

Crystal Data for **Zn-1**. $C_{474}H_{394}F_{48}N_{78}O_{66}S_{16}Zn_{14}$ $[Zn_8(C_{68}H_{44}N_{12}Zn)_6\cdot 16CF_3SO_3\cdot 6C_3NOH_7\cdot 8C_4H_{10}O\cdot 4H_2O]$, M = 10578.8, tetragonal, space group $P4/n$, black block, a = 34.401(5) Å, b = 34.401(5) Å, c = 27.321(4) Å, β = 90°, V = 32333(8) Å^3, Z = 2, D_c = 1.087 g cm^{-3}, μ(Mo Kα) = 0.633 mm^{-1}, T = 200(2) K, 28190 unique reflections [R_{int} = 0.0566], final R_1 [with $I > 2\sigma(I)$] = 0.0997, wR_2 (all data) = 0.2624 for 2θ = 50°, CCDC 2015811.

In the structural refinement of **Zn-1**, the non-H atoms were refined anisotropically and the H atoms were fixed geometrically at calculated distances and allowed to ride on the parent non-H atoms. The highly disordered state of the incorporated molecule solvents meant that lots of them could not be located, and hence in the final refinement, the electron density was treated with the *SQUEEZE* routine in the *PLATON* program package. The Zn center atoms and some of the C and N atoms in the porphyrin rings and several pyridine rings were disordered into two parts, with the s.o.f. of each part being refined using a free variable. To assist in the stability of the refinements, several restraints were applied: (1) Geometrical constraints of idealized regular polygons for the disordered pyridine rings in the ligand and coordinated DMF molecules were used. (2) Lots of atoms in the $CF_3SO_3^-$ anions were disordered, with the s.o.f. being fixed at suitable value. Many of the respective bond distances in the $CF_3SO_3^-$ anions and the solvent diethyl ether molecules were restrained to the idealized geometry. (3) The thermal parameters on adjacent atoms in some of the $CF_3SO_3^-$ anions were restrained to be similar. The A and B alerts in CheckCif were caused by the poor quality of the crystal resulting in weak diffraction intensities and the presence of disordered coordinated and free solvent molecules.

■ ASSOCIATED CONTENT

Supporting Information

The Supporting Information is available free of charge at https://pubs.acs.org/doi/10.1021/acs.inorgchem.1c00745.

Measurements and materials, preparation and characterizations, NMR data, NMR and IR spectra, UV−vis titrations, and kinetic analysis (PDF)

Accession Codes

CCDC 2015811 contains the supplementary crystallographic data for this paper. These data can be obtained free of charge via www.ccdc.cam.ac.uk/data_request/cif, or by emailing data_request@ccdc.cam.ac.uk, or by contacting The Cambridge Crystallographic Data Centre, 12 Union Road, Cambridge CB2 1EZ, UK; fax: +44 1223 336033.

■ AUTHOR INFORMATION

Corresponding Authors

Cheng He − *State Key Laboratory of Fine Chemicals, Dalian University of Technology, Dalian 116012, P. R. China;* orcid.org/0000-0002-1426-0124; Email: hecheng@dlut.edu.cn

Xin Liu − *State Key Laboratory of Fine Chemicals, Dalian University of Technology, Dalian 116012, P. R. China;* orcid.org/0000-0002-4422-4108; Email: xliu@dlut.edu.cn

Authors

LiLi Li − *State Key Laboratory of Fine Chemicals, Dalian University of Technology, Dalian 116012, P. R. China*

Linlin Yang − *Xinxiang Key Laboratory of Forensic Science Evidence, School of Forensic Medicine, Xinxiang Medical University, Xinxiang 453003, P. R. China*

Xuezhao Li − *State Key Laboratory of Fine Chemicals, Dalian University of Technology, Dalian 116012, P. R. China*

Jing Wang − *State Key Laboratory of Fine Chemicals, Dalian University of Technology, Dalian 116012, P. R. China*

Complete contact information is available at: https://pubs.acs.org/10.1021/acs.inorgchem.1c00745

Notes

The authors declare no competing financial interest.

https://doi.org/10.1021/acs.inorgchem.1c00745
Inorg. Chem. 2021, 60, 8802−8810

■ ACKNOWLEDGMENTS

This work was supported by the National Natural Science Foundation of China (Grants 21861132004, 21771029, and 21573034).

■ REFERENCES

(1) Zhao, L.; Jing, X.; Li, X. Z.; Guo, X. Y.; Zeng, L.; He, C.; Duan, C. Y. Catalytic Properties of Chemical Transformation within the Confined Pockets of Werner-Type Capsules. *Coord. Chem. Rev.* **2019**, *378*, 151−187.

(2) Ward, M. D.; Hunter, C. A.; Williams, N. H. Coordination Cages Based on Bis(pyrazolylpyridine) Ligands: Structures, Dynamic Behavior, Guest Binding, and Catalysis. *Acc. Chem. Res.* **2018**, *51*, 2073−2082.

(3) Fang, Y.; Powell, J. A.; Li, E. R.; Wang, Q.; Perry, Z.; Kirchon, A.; Yang, X. Y.; Xiao, Z. F.; Zhu, C. F.; Zhang, L. L.; Huang, F. H.; Zhou, H. C. Catalytic Reactions within the Cavity of Coordination Cages. *Chem. Soc. Rev.* **2019**, *48*, 4707−4730.

(4) Hong, C. M.; Bergman, R. G.; Raymond, K. N.; Toste, F. D. Self-Assembled Tetrahedral Hosts as Supramolecular Catalysts. *Acc. Chem. Res.* **2018**, *51*, 2447−2455.

(5) Leenders, S. H. A. M.; Gramage-Doria, R.; de Bruin, B.; Reek, J. N. H. Transition Metal Catalysis in Confined Spaces. *Chem. Soc. Rev.* **2015**, *44*, 433−448.

(6) Morimoto, M.; Bierschenk, S. M.; Xia, K. T.; Bergman, R. G.; Raymond, K. N.; Toste, F. D. Advances in Supramolecular Host-Mediated Reactivity. *Nat. Catal.* **2020**, *3*, 969−984.

(7) Gao, W. X.; Feng, H. J.; Lin, Y. J.; Jin, G. X. Covalent Post-Assembly Modification Triggers Structural Transformations of Borromean Rings. *J. Am. Chem. Soc.* **2019**, *141*, 9160−9164.

(8) Gao, W.-X.; Zhang, H.-N.; Jin, G.-X. Supramolecular Catalysis Based on Discrete Heterometallic Coordination-Driven Metallacycles and Metallacages. *Coord. Chem. Rev.* **2019**, *386*, 69−84.

(9) Li, H.; Han, Y. F.; Lin, Y. J.; Guo, Z. W.; Jin, G. X. Stepwise Construction of Discrete Heterometallic Coordination Cages Based on Self-Sorting Strategy. *J. Am. Chem. Soc.* **2014**, *136*, 2982−2985.

(10) Wei, J.; Zhao, L.; He, C.; Zheng, S.; Reek, J. N. H.; Duan, C. Metal-Organic Capsules with Nadh Mimics as Switchable Selectivity Regulators for Photocatalytic Transfer Hydrogenation. *J. Am. Chem. Soc.* **2019**, *141*, 12707−12716.

(11) Spicer, R. L.; Stergiou, A. D.; Young, T. A.; Duarte, F.; Symes, M. D.; Lusby, P. J. Host-Guest-Induced Electron Transfer Triggers Radical-Cation Catalysis. *J. Am. Chem. Soc.* **2020**, *142*, 2134−2139.

(12) Holloway, L. R.; Bogie, P. M.; Lyon, Y.; Ngai, C.; Miller, T. F.; Julian, R. R.; Hooley, R. J. Tandem Reactivity of a Self-Assembled Cage Catalyst with Endohedral Acid Groups. *J. Am. Chem. Soc.* **2018**, *140*, 8078−8081.

(13) Chen, S.; Li, K.; Zhao, F.; Zhang, L.; Pan, M.; Fan, Y. Z.; Guo, J.; Shi, J.; Su, C. Y. A Metal-Organic Cage Incorporating Multiple Light Harvesting and Catalytic Centres for Photochemical Hydrogen Production. *Nat. Commun.* **2016**, *7*, 13169.

(14) Rizzuto, F. J.; von Krbek, L. K. S.; Nitschke, J. R. Strategies for Binding Multiple Guests in Metal-Organic Cages. *Nat. Rev. Chem.* **2019**, *3*, 204−222.

(15) Hong, C. M.; Morimoto, M.; Kapustin, E. A.; Alzakhem, N.; Bergman, R. G.; Raymond, K. N.; Toste, F. D. Deconvoluting the Role of Charge in a Supramolecular Catalyst. *J. Am. Chem. Soc.* **2018**, *140*, 6591−6595.

(16) Kaphan, D. M.; Toste, F. D.; Bergman, R. G.; Raymond, K. N. Enabling New Modes of Reactivity Via Constrictive Binding in a Supramolecular-Assembly-Catalyzed Aza-Prins Cyclization. *J. Am. Chem. Soc.* **2015**, *137*, 9202−9205.

(17) Takezawa, H.; Shitozawa, K.; Fujita, M. Enhanced Reactivity of Twisted Amides inside a Molecular Cage. *Nat. Chem.* **2020**, *12*, 574−578.

(18) Yoshizawa, M.; Tamura, M.; Fujita, M. Diels-Alder in Aqueous Molecular Hosts: Unusual Regioselectivity and Efficient Catalysis. *Science* **2006**, *312*, 251−254.

(19) Marti-Centelles, V.; Lawrence, A. L.; Lusby, P. J. High Activity and Efficient Turnover by a Simple, Self-Assembled "Artificial Diels-Alderase". *J. Am. Chem. Soc.* **2018**, *140*, 2862−2868.

(20) Yoshizawa, M.; Takeyama, Y.; Kusukawa, T.; Fujita, M. Cavity-Directed, Highly Stereoselective [2 + 2] Photodimerization of Olefins within Self-Assembled Coordination Cages. *Angew. Chem., Int. Ed.* **2002**, *41*, 1347−1349.

(21) Nishioka, Y.; Yamaguchi, T.; Kawano, M.; Fujita, M. Asymmetric [2 + 2] Olefin Cross Photoaddition in a Self-Assembled Host with Remote Chiral Auxiliaries. *J. Am. Chem. Soc.* **2008**, *130*, 8160−8161.

(22) Cullen, W.; Misuraca, M. C.; Hunter, C. A.; Williams, N. H.; Ward, M. D. Highly Efficient Catalysis of the Kemp Elimination in the Cavity of a Cubic Coordination Cage. *Nat. Chem.* **2016**, *8*, 231−236.

(23) Fiedler, D.; Bergman, R. G.; Raymond, K. N. Supramolecular Catalysis of a Unimolecular Transformation: Aza-Cope Rearrangement within a Self-Assembled Host. *Angew. Chem., Int. Ed.* **2004**, *43*, 6748−6751.

(24) Yoshizawa, M.; Klosterman, J. K.; Fujita, M. Functional Molecular Flasks: New Properties and Reactions within Discrete, Self-Assembled Hosts. *Angew. Chem., Int. Ed.* **2009**, *48*, 3418−3438.

(25) Grommet, A. B.; Feller, M.; Klajn, R. Chemical Reactivity under Nanoconfinement. *Nat. Nanotechnol.* **2020**, *15*, 256−271.

(26) Kang, J. M.; Rebek, J. Acceleration of a Diels-Alder Reaction by a Self-Assembled Molecular Capsule. *Nature* **1997**, *385*, 50−52.

(27) Chen, J.; Rebek, J. Selectivity in an Encapsulated Cycloaddition Reaction. *Org. Lett.* **2002**, *4*, 327−329.

(28) Yoshizawa, M.; Takeyama, Y.; Okano, T.; Fujita, M. Cavity-Directed Synthesis within a Self-Assembled Coordination Cage: Highly Selective [2 + 2] Cross-Photodimerization of Olefins. *J. Am. Chem. Soc.* **2003**, *125*, 3243−3247.

(29) Murase, T.; Horiuchi, S.; Fujita, M. Naphthalene Diels-Alder in a Self-Assembled Molecular Flask. *J. Am. Chem. Soc.* **2010**, *132*, 2866−2867.

(30) Kuijpers, P. F.; Otte, M.; Durr, M.; Ivanovic-Burmazovic, I.; Reek, J. N. H.; de Bruin, B. A Self-Assembled Molecular Cage for Substrate-Selective Epoxidation Reactions in Aqueous Media. *ACS Catal.* **2016**, *6*, 3106−3112.

(31) Garcia-Simon, C.; Gramage-Doria, R.; Raoufmoghaddam, S.; Parella, T.; Costas, M.; Ribas, X.; Reek, J. N. H. Enantioselective Hydroformylation by a Rh-Catalyst Entrapped in a Supramolecular Metallocage. *J. Am. Chem. Soc.* **2015**, *137*, 2680−2687.

(32) Nurttila, S. S.; Becker, R.; Hessels, J.; Woutersen, S.; Reek, J. N. H. Photocatalytic Hydrogen Evolution by a Synthetic [Fefe] Hydrogenase Mimic Encapsulated in a Porphyrin Cage. *Chem. - Eur. J.* **2018**, *24*, 16395−16406.

(33) Colomban, C.; Fuertes-Espinosa, C.; Goeb, S.; Salle, M.; Costas, M.; Blancafort, L.; Ribas, X. Self-Assembled Cofacial Zinc-Porphyrin Supramolecular Nanocapsules as Tuneable $^1O_2$ Photosensitizers. *Chem. - Eur. J.* **2018**, *24*, 4371−4381.

(34) Zhu, H. T. Z.; Li, Q.; Shi, B. B.; Ge, F. J.; Liu, Y. Z.; Mao, Z. W.; Zhu, H.; Wang, S.; Yu, G. C.; Huang, F. H.; Stang, P. J. Dual-Emissive Platinum(II) Metallacage with a Sensitive Oxygen Response for Imaging of Hypoxia and Imaging-Guided Chemotherapy. *Angew. Chem., Int. Ed.* **2020**, *59*, 20208−20214.

(35) Smith, P. T.; Benke, B. P.; Cao, Z.; Kim, Y.; Nichols, E. M.; Kim, K.; Chang, C. J. Iron Porphyrins Embedded into a Supramolecular Porous Organic Cage for Electrochemical CO_2 Reduction in Water. *Angew. Chem., Int. Ed.* **2018**, *57*, 9684−9688.

(36) Smith, P. T.; Kim, Y.; Benke, B. P.; Kim, K.; Chang, C. J. Supramolecular Tuning Enables Selective Oxygen Reduction Catalyzed by Cobalt Porphyrins for Direct Electrosynthesis of Hydrogen Peroxide. *Angew. Chem., Int. Ed.* **2020**, *59*, 4902−4907.

(37) Meng, W.; Breiner, B.; Rissanen, K.; Thoburn, J. D.; Clegg, J. K.; Nitschke, J. R. A Self-Assembled M_8L_6 Cubic Cage That Selectively Encapsulates Large Aromatic Guests. *Angew. Chem., Int. Ed.* **2011**, *50*, 3479−3483.

https://doi.org/10.1021/acs.inorgchem.1c00745
Inorg. Chem. 2021, 60, 8802−8810

(38) Percastegui, E. G.; Mosquera, J.; Nitschke, J. R. Anion Exchange Renders Hydrophobic Capsules and Cargoes Water-Soluble. *Angew. Chem., Int. Ed.* **2017**, *56*, 9136−9140.
(39) Rizzuto, F. J.; Nitschke, J. R. Narcissistic, Integrative, and Kinetic Self-Sorting within a System of Coordination Cages. *J. Am. Chem. Soc.* **2020**, *142*, 7749−7753.
(40) Deria, P.; Gomez-Gualdron, D. A.; Hod, I.; Snurr, R. Q.; Hupp, J. T.; Farha, O. K. Framework-Topology-Dependent Catalytic Activity of Zirconium-Based (Porphinato)zinc(II) MOFs. *J. Am. Chem. Soc.* **2016**, *138*, 14449−14457.
(41) Mondal, P.; Sarkar, S.; Rath, S. P. Cyclic Bis-Porphyrin-Based Flexible Molecular Containers: Controlling Guest Arrangements and Supramolecular Catalysis by Tuning Cavity Size. *Chem. - Eur. J.* **2017**, *23*, 7093−7103.
(42) Oliveri, C. G.; Gianneschi, N. C.; Nguyen, S. T.; Mirkin, C. A.; Stern, C. L.; Wawrzak, Z.; Pink, M. Supramolecular Allosteric Cofacial Porphyrin Complexes. *J. Am. Chem. Soc.* **2006**, *128*, 16286−16296.
(43) Shultz, A. M.; Farha, O. K.; Hupp, J. T.; Nguyen, S. T. A Catalytically Active, Permanently Microporous MOF with Metalloporphyrin Struts. *J. Am. Chem. Soc.* **2009**, *131*, 4204−4205.
(44) Benda, L.; Doistau, B.; Rossi-Gendron, C.; Chamoreau, L.-M.; Hasenknopf, B.; Vives, G. Substrate-Dependent Allosteric Regulation by Switchable Catalytic Molecular Tweezers. *Commun. Chem.* **2019**, *2*, 144.
(45) Huang, S.; Lin, Y.; Hor, T.; Jin, G. Cp*Rh-Based Heterometallic Metallarectangles: Size-Dependent Borromean Link Structures and Catalytic Acyl Transfer. *J. Am. Chem. Soc.* **2013**, *135*, 8125−8128.
(46) Mackay, L. G.; Wylie, R. S.; Sanders, J. K. M. Catalytic Acyl Transfer by a Cyclic Porphyrin Trimer-Efficient Turnover without Product Inhibition. *J. Am. Chem. Soc.* **1994**, *116*, 3141−3142.
(47) Zhang, W.; Dynes, J. J.; Hu, Y.; Jiang, P.; Ma, S. Porous Metal-Metalloporphyrin Gel as Catalytic Binding Pocket for Highly Efficient Synergistic Catalysis. *Nat. Commun.* **2019**, *10*, 1913.
(48) Collins, J. B.; Schleyer, P. V. R.; Binkley, J. S.; Pople, J. A. Self-Consistent Molecular-Orbital Methods. XVII. Geometries and Binding-Energies of 2nd-Row Molecules-Comparison of 3 Basis Sets. *J. Chem. Phys.* **1976**, *64*, 5142−5151.
(49) Hehre, W. J.; Stewart, R. F.; Pople, J. A. Self-Consistent Molecular-Orbital Methods.I. Use of Gaussian Expansions of Slater-Type Atomic Orbitals. *J. Chem. Phys.* **1969**, *51*, 2657−2664.
(50) Hay, P. J.; Wadt, W. R. Abinitio Effective Core Potentials for Molecular Calculations - Potentials for the Transition-Metal Atoms Sc to Hg. *J. Chem. Phys.* **1985**, *82*, 270−283.
(51) Wadt, W. R.; Hay, P. J. Abinitio Effective Core Potentials for Molecular Calculations - Potentials for Main Group Elements Na to Bi. *J. Chem. Phys.* **1985**, *82*, 284−298.
(52) Hay, P. J.; Wadt, W. R. Abinitio Effective Core Potentials for Molecular Calculations - Potentials for K to Au Including the Outermost Core Orbitals. *J. Chem. Phys.* **1985**, *82*, 299−310.
(53) Becke, A. D. Density-Functional Thermochemistry. III. The Role of Exact Exchange. *J. Chem. Phys.* **1993**, *98*, 5648−5652.
(54) Lee, C. T.; Yang, W. T.; Parr, R. G. Development of the Colle-Salvetti Correlation-Energy Formula into a Functional of the Electron-Density. *Phys. Rev. B: Condens. Matter Mater. Phys.* **1988**, *37*, 785−789.
(55) Frisch, M. J.; Trucks, G. W.; Schlegel, H. B.; Scuseria, G. E.; Robb, M. A.; Cheeseman, J. R.; Scalmani, G.; Barone, V.; Petersson, G. A.; Nakatsuji, H.; Li, X.; Caricato, M.; Marenich, A. V.; Bloino, J.; Janesko, B. G.; Gomperts, R.; Mennucci, B.; Hratchian, H. P.; Ortiz, J. V.; Izmaylov, A. F.; Sonnenberg, J. L.; Williams, D. F.; Lipparini, F.; Egidi, F.; Goings, J.; Peng, B.; Petrone, A.; Henderson, T.; Ranasinghe, D.; Zakrzewski, V. G.; Gao, J.; Rega, N.; Zheng, G.; Liang, W.; Hada, M.; Ehara, M.; Toyota, K.; Fukuda, R.; Hasegawa, J.; Ishida, M.; Nakajima, T.; Honda, Y.; Kitao, O.; Nakai, H.; Vreven, T.; Throssell, K.; Montgomery, J. A., Jr.; Peralta, J. E.; Ogliaro, F.; Bearpark, M. J.; Heyd, J. J.; Brothers, E. N.; Kudin, K. N.; Staroverov, V. N.; Keith, T. A.; Kobayashi, R.; Normand, J.; Raghavachari, K.; Rendell, A. P.; Burant, J. C.; Iyengar, S. S.; Tomasi, J.; Cossi, M.; Millam, J. M.; Klene, M.; Adamo, C.; Cammi, R.; Ochterski, J. W.; Martin, R. L.; Morokuma, K.; Farkas, O.; Foresman, J. B.; Fox, D. J. *Gaussian 16*, revision A.03; Gaussian Inc.: Wallingford, CT, 2016.
(56) Kuzmic, P. Program Dynafit for the Analysis of Enzyme Kinetic Data: Application to Hiv Proteinase. *Anal. Biochem.* **1996**, *237*, 260−273.
(57) *SMART Data Collection Software*, version 5.629; Bruker AXS Inc.: Madison, WI, 2003.
(58) *SAINT Data Reduction Software*, version 6.45; Bruker AXS Inc.: Madison, WI, 2003.
(59) Sheldrick, G. M. Crystal Structure Refinement with Shelxl. *Acta Crystallogr., Sect. C: Struct. Chem.* **2015**, *C71*, 3−8.

https://doi.org/10.1021/acs.inorgchem.1c00745
Inorg. Chem. 2021, 60, 8802−8810